NUREG/CR-0088
ANL-77-80

NUREG/CR-0088
ANL-77-80

FISSION-GAS RELEASE FROM IRRADIATED PWR FUEL DURING SIMULATED PCM-TYPE ACCIDENTS: PROGRESS REPORT

by

S. M. Gehl, M. G. Seitz, and J. Rest

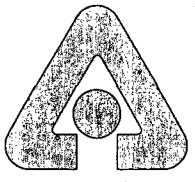

ARGONNE NATIONAL LABORATORY, ARGONNE, ILLINOIS

Prepared for the U. S. NUCLEAR REGULATORY COMMISSION
under Interagency Agreement DOE 40-550-75

Available from
National Technical Information Service
Springfield, Virginia 22161

NUREG/CR-0088
ANL-77-80

Distribution Code: R-3

ARGONNE NATIONAL LABORATORY
9700 South Cass Avenue
Argonne, Illinois 60439

FISSION-GAS RELEASE FROM IRRADIATED PWR FUEL DURING SIMULATED PCM-TYPE ACCIDENTS: PROGRESS REPORT

by

S. M. Gehl, M. G. Seitz, and J. Rest

Materials Science Division

Manuscript Submitted: June 1977
Date Published: May 1978

Prepared for
Division of Water Reactor Safety Research
U. S. Nuclear Regulatory Commission
Washington, D.C. 20555
Under Interagency Agreement DOE 40-550-75

NRC FIN No. A2016

TABLE OF CONTENTS

LIST OF FIGURES

LIST OF FIGURES

LIST OF TABLES

FISSION-GAS RELEASE FROM IRRADIATED PWR FUEL DURING SIMULATED PCM-TYPE ACCIDENTS: PROGRESS REPORT

by

S. M. Gehl, M. G. Seitz, and J. Rest

ABSTRACT

Radial temperature profiles and centerline heating rates of hypothetical power-cooling-mismatch accidents were simulated in irradiated commercial pressurized-water-reactor fuel with a direct-electrical-heating technique. The fission-gas release, transient temperature histories, and transient-induced microstructural changes were determined for these experiments. Empirical relationships were developed between gas release and the maximum centerline temperature and between gas release and the maximum volume-averaged temperature gradient. Preliminary conclusions were made about the mechanisms of gas release, based on the transient-induced microstructural changes and a comparison of measured gas releases with the predictions of a mechanistic computer code, GRASS-SST.

Intergranular fission-gas bubbles, grain-surface channels, grain-edge tunnels, and intergranular separations were formed during the transients. The long-range interlinkage of these features provided pathways for the escape of fission gas that diffused to the grain boundaries. A relationship was developed between gas release and the extent of microstructural change, as expressed by the volume swelling. Both diffusion-controlled (bubble growth and coalescence) and mechanical (cracking) mechanisms were found to be important in determining the transient gas release.

I. INTRODUCTION

The importance of fission-gas behavior in light-water-reactor safety studies stems from two considerations: (1) the possible release of large amounts of radioactive krypton, xenon, and iodine gas to the environment as a result of the breaching of the fuel-rod cladding during postulated accident situations, and (2) the need to determine whether a fuel rod may be operated safely after a transient in which gas release occurs but cladding rupture does

not. Although the empirical models used by manufacturers for predicting gas release during normal operation are adequate for licensing analyses, there is considerable uncertainty as to the expected gas release during transients.[1] This situation is partly a result of the uncertainties in fuel-temperature measurement that lead to large variances in release fraction for existing gas-release data.[1,2]

The Argonne National Laboratory (ANL) Transient Fuel Response and Fission-product Release Program is supplying needed gas-release data by performing well-characterized out-of-reactor transient heating experiments on irradiated commercial reactor fuel. Radial temperature profiles similar to those of nuclear heating are produced in the fuel by the direct-electrical-heating (DEH) technique.[3] This heating method provides the capability for controlled variation of the heating rate and radial temperature gradient over wide ranges and, consequently, the capability to simulate a variety of accident conditions. Correlations of the measured gas release with the transient temperature history are used for verifying the models used in a mechanistic computer code, Steady State and Transient Gas-release and Swelling Subroutine (GRASS-SST),[4] which is being developed for the Nuclear Regulatory Commission by ANL. Detailed examinations of the microstructural changes and fission-gas-bubble morphology produced during the transients are used to determine the mechanisms responsible for gas release and, where necessary, to indicate the need for modeling additional phenomena in the GRASS-SST code.

The overall program at ANL is concerned with the release of gaseous and volatile fission products during hypothetical power-cooling-mismatch (PCM) accidents, loss-of-coolant accidents (LOCA's), and reactivity-initiated accidents (RIA's). The present report describes the gas-release results obtained from an initial series of PCM simulations. Experimental correlations of gas release with thermal test conditions and with the microstructural changes caused by transient heating are described. In addition, the experimentally measured gas releases are compared with the predictions of the GRASS-SST code.

II. EXPERIMENTAL PROCEDURE

A. Material

The fuel used for the initial series of PCM tests was taken from a bundle of commercial pressurized-water-reactor (PWR) fuel rods irradiated in the H. B. Robinson No. 2 Reactor. The fuel, fabricated by Westinghouse, had an initial density of 92% of theoretical and an initial ^{235}U enrichment of 2.55 wt %. The fuel pellets were 15 mm long and 9.3 mm in diameter and had dished ends. Axial flux-shape histories for the Robinson irradiations indicate that the average linear heat-generation rates (LHGR's) were 22.4 and 17.7 kW/m

in the first and second cycles, respectively.[5] The ratio of peak-to-average LHGR was ~1.3 to 1. Two rods from the same bundle had postirradiation helium pressures of ~1.4 MPa at 25°C.[6] The fission gas released to the gap and plenum of these rods represented ~0.2% of the amount generated during irradiation.[6]

The fuel pellets used for the present experiments were taken from rods F-7 and G-6 of the bundle. Table I lists burnup analyses (as determined from mass-spectrometric measurements of ^{148}Nd) for three axial positions in rod F-7. Burnup values for fuel from other axial positions were estimated by normalizing the axial profile of gross gamma activity to a maximum burnup of 3.14 at. %.

TABLE I. Burnup Analysis of Robinson Rod F-7

Sample Identity	Distance from Rod Bottom, m	U, g	^{148}Nd, μg	Burnup, at. %
155AA8	0.006	2.9072	389.8	1.26
155AA7	0.57	2.0758	706.2	3.14
155AA3	0.93	1.9152	648.5	3.12

The fission-gas content of the fuel was determined by dissolving an ~9-g fuel specimen from the high-burnup central plateau of rod F-7 and collecting the fission gas released by the dissolution. The fission gas generated and retained within the fuel during irradiation was determined to be 0.685 cm^3 (STP) of xenon per gram of fuel and 0.053 cm^3 (STP) of krypton per gram of fuel. The isotopic content of the gas is given in Table II.

TABLE II. Isotopic Analysis of Fission Gas in Robinson Fuel

Xenon			Krypton		
Isotope[a]	Concentration, %	Accuracy	Isotope	Concentration, %	Accuracy
128	0.03	±0.01	83	11.4	±0.3
130	0.14	±0.02	84	31.2	±0.4
131	8.0	±0.2	85	6.0	±0.3
132	20.5	±0.3	86	51.3	±0.3
134	28.1	±0.3			
136	43.3	±0.4			

[a]A detectable amount of an isotope of mass 129, which is possibly ^{129}I, was also present.

B. The Direct-electrical-heating Technique

Direct electrical heating (DEH) of nuclear reactor fuel and unirradiated UO_2 has evolved as a technique well suited to the study of fuel and fission-product behavior under transient-heating conditions. Compared to in-reactor

transient tests, the DEH technique has the advantages of good specimen visibility, ease of instrumenting the test specimen, ease of collection and measurement of gas release for a single pellet, the capability to vary power input independently of fuel enrichment, and relatively low cost.

There are limitations to the DEH technique. For example, like other simulation methods, it is necessary to determine whether, and to what extent, the nonprototypicalities inherent in the DEH technique affect the results. This question is discussed in Sec. IV.B. Also, there are difficulties in preparing test specimens, as discussed in Sec. II.D.

In the DEH technique, electric current is passed through a stack of pellets in the axial direction. The ohmic heating of the UO_2 and the radial heat loss to the helium coolant produce a radial temperature profile that approximates the profiles obtained for nuclear heating. The electronic control circuitry of the apparatus used for the present experiments is capable of varying the power-input levels and power-ramp rates over wide ranges to simulate the temperature profiles of a variety of nuclear heating conditions. The design of the power supplies and control circuitry is based on equipment described by Wrona and Johanson.[7]

C. Transient-heating Apparatus

The chamber used for the DEH experiments is shown schematically in Fig. 1. A stack of pellets is held vertically between two tungsten electrodes.

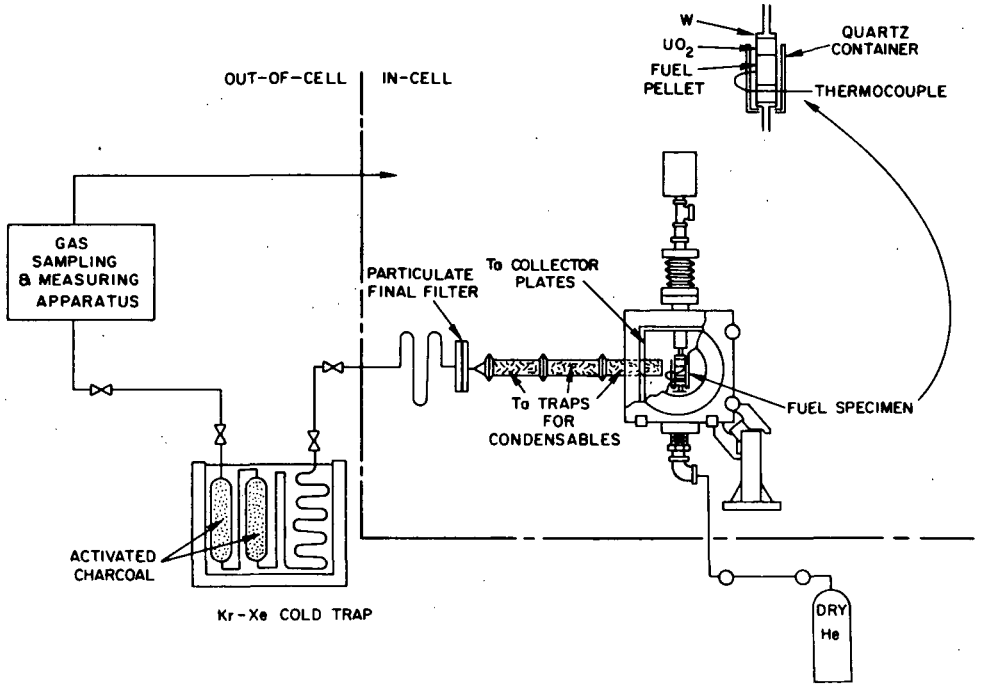

Fig. 1. Schematic Design of In-cell DEH and Fission-product Collection Apparatus. Neg. No. MSD-64434.

The bottom electrode is fixed, but the upper electrode is free to slide vertically. An axial load of ~200 g is applied to the pellet stack through the movable upper electrode. This mass, equivalent to a stack of fuel pellets ~0.3 m high, simulates the accumulated load on a typical pellet in a fuel rod. The specimen chamber incorporates a quartz window for viewing the specimen and surface-temperature measurement by optical pyrometry, a removable tantalum liner for collecting condensable fission products, and feedthroughs for thermocouples that contact the specimen surface.

Three streams of helium coolant flow through the chamber during DEH tests. Two of the streams enter at the top and bottom electrodes; the third stream strikes the quartz window at a glancing angle, thus preventing fission products from depositing on the window and obscuring the view. The helium stream exits through a port in the left side of the chamber, passes through a tantalum raschig-ring trap, two paper-element filters, and a millipore filter to collect all condensables and particulates.

The fission gases carried along with the flowing helium stream are collected by passing the gas through an activated charcoal trap cooled by liquid nitrogen. After each test the trapped gases, representing the cumulative total released during the test, are recovered by heating the charcoal. The total amount of gas collected, its chemical composition, and the krypton and xenon isotopic composition are then determined.

D. Specimen Preparation

The thermal shock accompanying reactor startup and shutdown produces a network of large cracks in oxide fuels. Because of the low irradiation temperatures experienced by the Robinson fuel, crack healing did not occur. As a result, in their postirradiation state, the individual pellets were divided into 5-20 fragments held in place by the Zircaloy cladding. If the cladding were to be left in place for DEH tests, it would provide a higher conductivity path for the electric current and prevent heating of the fuel. Because the cladding must be removed before DEH testing, an alternative means was needed for retaining the cylindrical geometry of the fuel pellets and fixing the relative positions of the fragments. In addition, early tests indicated that the displacement of pellet fragments during irradiation and handling frequently result in adjacent fragments contacting each other at a few isolated points. This point contact usually means that the fragments are in poor electrical contact. A specimen-preparation technique was developed that was successful in producing usable DEH specimens from the fragmented Robinson fuel pellets.

The specimen-preparation procedure is based on the use of a UO_2 slip that fills some of the free space between pellet fragments, thereby incorporating all the pieces into the electrical circuit and preventing relative motion of the fragments. The slip is a suspension of fine UO_2 powder (~0.6-μm particle diameter) in an aqueous solution of organic binders. The slip composition is given in Table III.[8]

TABLE III. Composition of UO_2 Slip[8]

0.6-μm depleted UO_2 powder, g	400	Distilled water, mL	300
Ammonium alginate,[a] g	2.0	Ammonium hydroxide, drops	15
Hydroxypropyl methylcellulose,[b] g	2.0		

[a]Kelco Superloid.
[b]Dow Methocel F4M.

Sections of clad fuel ~150 mm in length are impregnated with slip using the apparatus shown in Fig. 2. One end of the fuel section is connected, by means of a compression fitting, to a lever-actuated grease gun; a vacuum line is connected to the other end. The grease gun is used to pump slip into pellet interfaces and cracks, and into the gap between the fuel and cladding. The clad fuel is evacuated before the slip is injected to prevent the formation of trapped air pockets that might expand and drive the slip out of the cracks when the injection pressure is released. The impregnated fuel lengths are allowed to dry for ~2 days in air at room temperature and are then cut into a number of smaller pieces, each containing a single pellet.

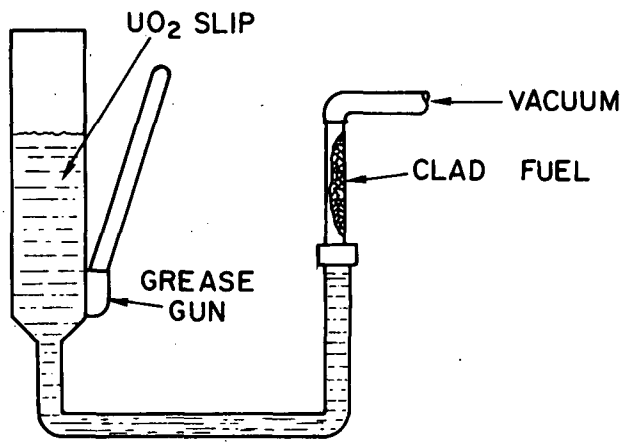

Fig. 2. Schematic of Slip-impregnation Apparatus. Neg. No. MSD-62086.

The next step in the specimen-preparation procedure is the removal of the Zircaloy cladding sections from the pellets. Since there is no metallurgical bonding of the cladding to the fuel in the Robinson fuel rods, the cladding can be slid off the fuel while flat-ended cylindrical rods hold the pellet ends fixed and parallel. Limited success has been achieved in producing free-standing pellets in this way. However, the pellets are fragile, making remote handling difficult.

To reduce breakage, a flat-bottomed quartz tube is slid in place around the pellet as the cladding is slid off. The quartz tube, shown schematically in Fig. 1, and before and after testing in Fig. 3, is loaded with a tungsten disk (to form the bottom electrode) and an unirradiated depleted-UO_2 pellet before the fuel is introduced.

A second unirradiated depleted pellet is placed in the tube on top of the fuel pellet. The tube protects the fuel during all handling operations and is left in place during transient testing. The tube fits loosely around the fuel pellet to permit the escape of fission gases. The tube does not supply radial constraint to the fuel. Two holes in the tube wall permit thermocouples to be placed in contact with the fuel for direct temperature measurement. The tungsten rod of the lower electrode extends through a hole in the base of the quartz tube.

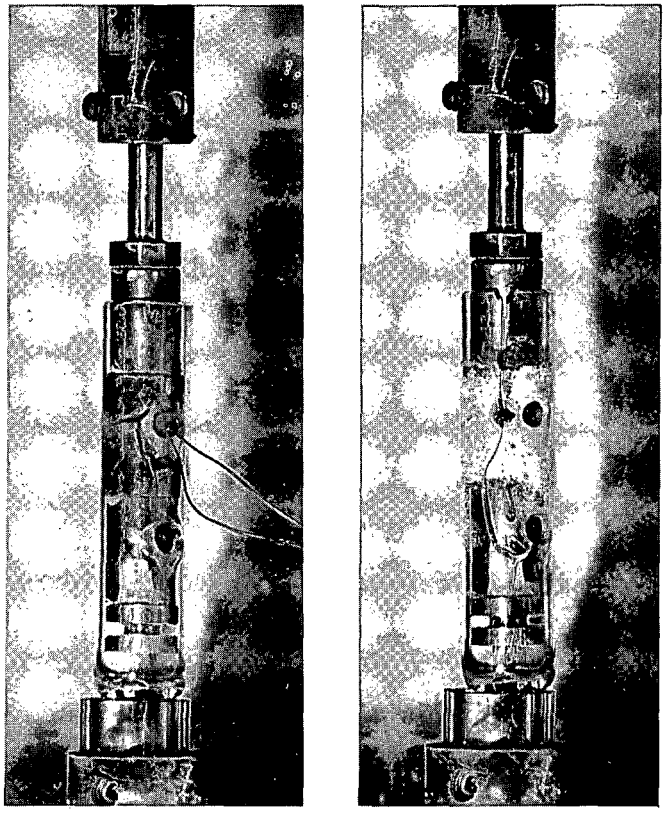

A. Before DEH Testing B. After DEH Testing

Fig. 3

DEH Specimen Test Assembly before and after a Transient Test. A. Neg. No. MSD-188774; B. MSD-188775.

The initial attempts at DEH testing of slip-impregnated pellets indicated that the rapid vaporization of the retained water and the organic compounds in the slip generated forces sufficient to dislodge pellet fragments and crack the quartz tube. A slow heating schedule using a focused line heater was developed to prevent disruption of the pellet stack by ensuring that the volatilization of retained water and organic compounds is a gradual process. The line heater, located outside the specimen chamber, heats the specimen through the front window of the chamber. During an ~90-min period of the preheat schedule, the specimen temperature is raised from ambient to ~300°C as measured by the fuel-surface thermocouple. The 300°C temperature is maintained for an additional 30 min. This temperature is sufficient to volatilize the water and organics, but is low enough to prevent thermal decomposition of the organics and movement of fission gas.

III. RESULTS

The initial series of PCM thermal-transient simulations consisted of 16 DEH tests. The experimental conditions and gas releases for these tests are listed in Table IV. In tests 9, 16, 18, 21, 25, and 26, the transients were run to produce small melt fractions. Incipient melting occurred at the center of the fuel in test 24. The melt radii gave unequivocal indications of the local maximum temperatures, which were used for calibrating the calculations of transient temperature histories. The fractional gas releases from the melt zones are not known. However, because of the small sizes of the melt zones (1-11% of the fuel volume) gas releases from the liquid portions were small compared to the corresponding overall gas releases.

Some of the fission products were vaporized during the transient heating and condensed on the inner surface of the quartz tube opposite the high-burnup fuel forming a silvery deposit, shown in Fig. 3B. The deposit did not form opposite the depleted-UO_2 pellets. Radiochemical analysis of the deposit indicated the presence of ^{106}Ru, ^{134}Cs, ^{137}Cs, and ^{144}Ce.

In test 31, the fuel was subjected to a steady-state power input of 500 W for ~15 min before transient heating was initiated. Surface temperatures reached 1270°C during the steady-state heating. In all other tests, the pretransient power was held to 300 W or less. Calculations of the pretransient and transient temperature histories of test 31 have not been completed.

A few notes are necessary to explain some of the entries in Table IV. Because of problems with the power-control circuitry, the power ramp experienced by the test specimen usually differed somewhat from the programmed ramp. The columns headed "Power Ramp" (Programmed and Actual) permit an evaluation of these differences.

The confidence intervals indicated for the xenon release values were obtained by assuming a possible error of plus or minus one in the least significant digit of the gas-sample chemical analysis. Other sources of uncertainty, due to possible errors in calibrating the volume of the gas-measuring and -sampling system and in reading the pressure of the gas recovered from the charcoal, were insignificant compared to the assumed errors in the chemical analyses.

Gas release was also calculated as a percentage of the amount present in the fuel at the end of irradiation. Retained gas concentrations of 0.685 and 0.053 cm^3/g for xenon and krypton, respectively, as determined by whole-pellet dissolution, were corrected for axial burnup variations and used for calculating the percentage released.

Figure 4, a plot of xenon release as a function of total energy for all PCM-type DEH tests, shows that there is a general trend of higher gas-release

TABLE IV. Experimental Conditions and Gas Releases for PCM-type Tests

Test No.	Spec. No. 155-	Duration of Test, s	Power Ramp, W/s		Integrated Power, 10^4 W·s	Avg. CL Heat Rate, °C/s	Xenon Release		Krypton Release		Estimated Gas Release from Unmelted Fuel,[a] %	
			Programmed	Actual			cm^3/g	%[b]	cm^3/g	%[b]	Xenon	Krypton
9	AC18	15	500	500	1.40	430	0.08	12				
16	AC25	9	60	67	0.64	200	0.01	2	0.003	6		
18	AC26	31	7.5	21	1.88	80	0.05	8	0.008	16		
21	AC27	68	4.0	10	3.16	25	0.320 ± 0.007	50.0 ± 1.0	0.030	60	44 ± 1	55
22	AD6	36	4.0	7.3	1.64	36	0.085 ± 0.003	13.1 ± 0.5	0.012	25		
23	AD18	28	4.0	7.3	1.17	41	0.006-0.030	1-5	0.001-0.005	2-10		
24	AD29	50	4.0	8.4	2.54	28	0.082 ± 0.003	12.0 ± 0.5	0.016	30		
25	AD40	58	4.0	10	3.38	25	0.162 ± 0.015	43.0 ± 3.9	0.021	72	36 ± 4	68
26	CC4	54	4.0	2.1	4.32	15	0.427 ± 0.011	63.1 ± 1.6	0.032	61	59 ± 2	57
27	CC3	54	4.0	7.4	3.24	22	0.225 ± 0.004	33.3 ± 0.7	0.033	63		
28	CC5	50	4.0	6.8	2.55							
29	CC11	59	4.0	4.5	2.50	12	0.014 ± 0.004	2.0 ± 0.6	0.002	4		
30	CC6	70	4.0	0.7	1.46	10	0.003 ± 0.001	0.4 ± 0.1	4×10^{-4}	0.8		
31	CC13	71	4.0	12	6.17		0.141 ± 0.011	20.1 ± 1.5	0.010	19		
32	CC14	60	4.0	5.5	2.59	22	0.110 ± 0.016	16.1 ± 2.4	0.008	15		
33	CC15	100	4.0	5.0	4.14	12	0.292 ± 0.015	42.6 ± 2.2	0.026	49		

[a]Assuming that the liquid fuel released its entire gas burden.
[b]Corrected for burnup and normalized to pretest xenon and krypton contents of 0.685 and 0.053 cm^3/g, respectively.

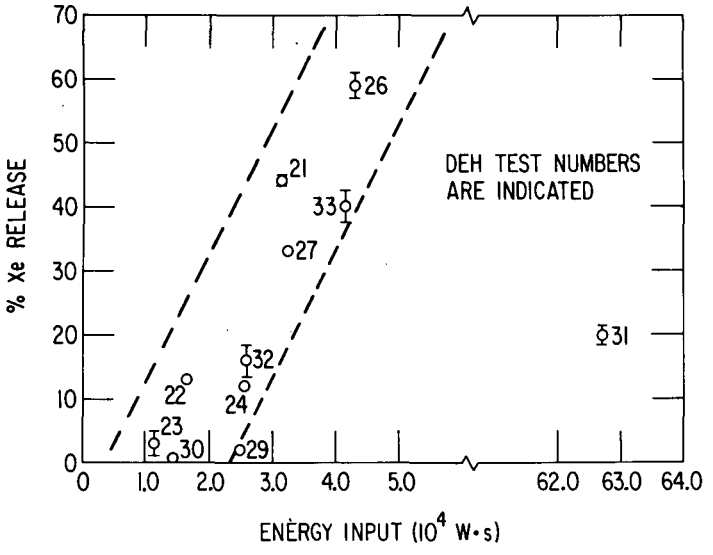

Fig. 4. Xenon Release as a Function of Total Energy for PCM-type DEH Tests. Neg. No. MSD-64912-R.

fractions at higher total power depositions. Test 31 shows the only large deviation from the trend indicated by the parallel dashed lines in Fig. 4. This deviation may be due to the long, high-power pretransient heating in test 31. The details of the thermal history must be examined to explain the apparent scatter in the data for the other tests.

The entries in the column headed "Estimated Gas Release from Unmelted Fuel" are estimates of the gas released from the unmelted portions of specimens in which central melting occurred. The estimates, obtained under the limiting assumption that 100% of the gas originally contained in the melt zones was released, are only slightly smaller than the corresponding overall release values. The actual release fractions from melted fuel lie between the overall release values and the limiting value of 100%. Similarly, the release from unmelted fuel is intermediate to the overall release and the values calculated for 100% release from the liquid. Although direct evidence of the retained gas in melted fuel is unavailable, the indirect evidence of the posttest microstructures suggests that nearly all the gas escaped from this region.

A transverse section through the fuel pellet transient-tested to melting in test 26 is shown in Fig. 5. The central melt zone contains bubbles in the

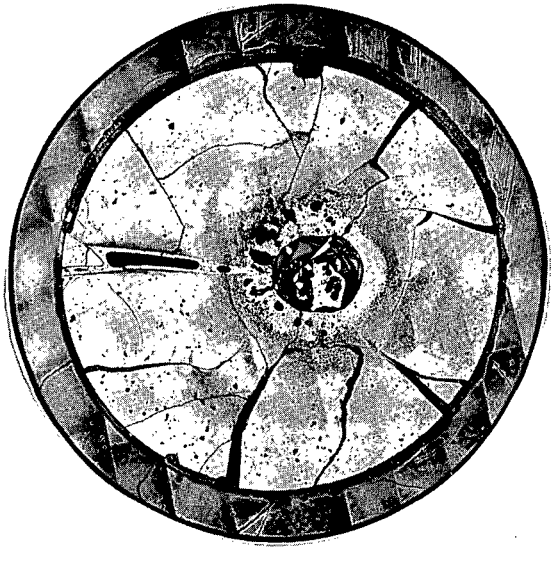

Fig. 5

Transverse Section through Robinson Fuel Pellet after Test 26. Neg. No. MSD-189963.

size range 0.02-0.5 mm. The large size of these features, compared to bubbles in solid fuel, is a result of the extremely rapid coalescence and growth rates of bubbles in liquid fuel. Most of the gas in bubbles of this type is likely to have been vented to the outside, either by percolation of the bubbles through the liquid, or via the cracks that formed during cooldown following solidification.

A. Relationships between Gas Release and Transient-temperature History

1. Parameters for Describing Temperature History

Radial temperature profiles are calculated as a function of time during DEH tests with the DEH Transient Temperature Distribution (DEHTTD) code.[9] The calculational procedure and the possible sources of error in the calculated temperatures are discussed in the appendix. The radial temperature profiles of test 24, plotted in Fig. 6 for both the heating and cooling portions of a transient, show the general trends observed for all tests. Both centerline and surface temperature increased monotonically during the power-on portion of the transient. Since the centerline temperature increased more rapidly than the surface temperature, the volume-averaged temperature gradient increased during this portion of the transient. After the power was turned off, the centerline temperature decreased more rapidly than the surface temperature, and the temperature gradient also decreased.

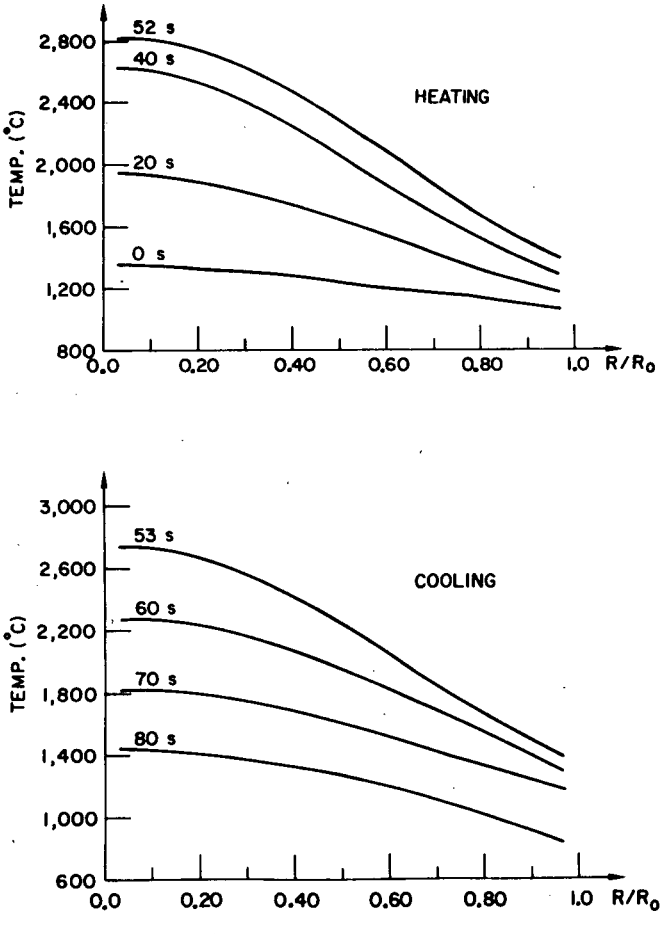

Fig. 6. Time Sequence of Radial Temperature Profiles for Test 24. Neg. No. MSD-64420.

To develop relationships between gas release and thermal conditions, the complex temperature behavior shown in Fig. 6 was described with a set of simplified parameters. The quantities used for this purpose included time integrals of temperature and temperature gradient, referred to as integral parameters, and terms that express the extremes in temperature and temperature gradient, called maximum parameters. A partial list of the parameters considered and the notation used for this representation are given in Table V. Because of the similarity in test conditions

for the present series of DEH experiments, relationships were discovered between parameters that are, in principle, mutually independent. These relationships greatly reduced the number of independent parameters needed to describe the temperature histories.

TABLE V. Parameters Used to Describe Transient Thermal History

Integral Parameters	1a.	$\int_p \overline{T}\, dt$	Time integral of volume-averaged temperature, powered portion of transient only
	1b.	$\int_t \overline{T}\, dt$	Time integral of volume-averaged temperature, total transient
	2.	$\int T_{CL}\, dt$[a]	Time integral of centerline temperature
	3.	$\int (\overline{dT/dR})dt$[a]	Time integral of volume-averaged radial temperature gradient
Maximum Parameters	4.	$T_{CL_{max}}$	Maximum centerline temperature
	5.	$(\overline{dT/dR})_{max}$	Maximum volume-averaged temperature gradient

[a]These integrals may be evaluated separately for the powered portion and the totality of the transient as shown for items 1a and 1b.

As an example, the relationship between two of the integral parameters is presented in Fig. 7, in which $\int(\overline{dT/dR})dt$ is plotted against $\int \overline{T}\, dt$ for nine DEH tests. The integrals were evaluated separately for the heating and cooling portions of the transients. Both sets of data can be described by a single straight line passing through the origin. Relationships of this type were found among all of the integral parameters.

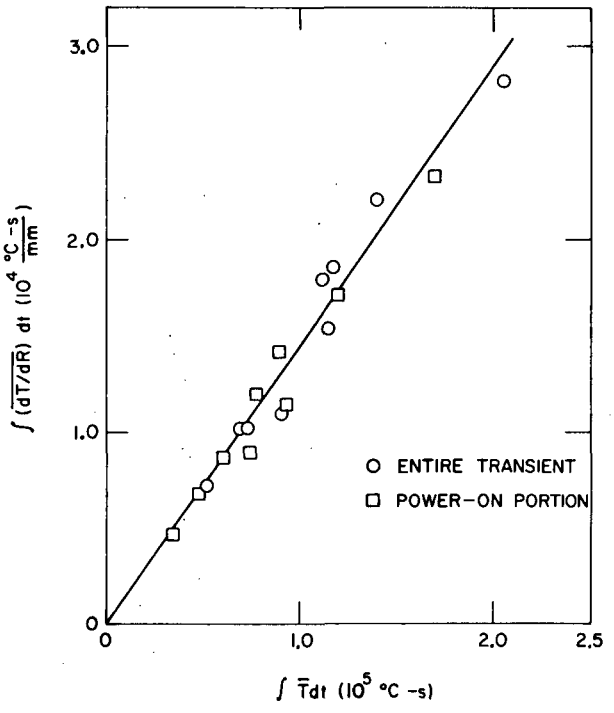

Fig. 7. Relationship between Time Integrals of Volume-averaged Temperature and Temperature Gradient for PCM-type Tests. ANL Neg. No. 306-77-314.

Similarly, as shown in Fig. 8, there is a relationship between the maximum parameters, $(\overline{dT/dR})_{max}$ and $T_{CL_{max}}$. However, a plot of $(\overline{dT/dR})_{max}$ versus $\int_p \overline{T}\, dt$ (Fig. 9) shows that the maximum parameters are nearly independent of the integral parameters. Therefore, the transient-temperature histories can be fully described by two nearly independent parameters, one selected from the group of integral parameters and one from the maximum parameters.

The small number of independent thermal-history parameters is due to

similarity in test conditions. For tests that cover a wider range of initial conditions and heating rates, a larger number of parameters would be independent. As the range of test conditions is expanded, other parameters may be determined to be more useful for correlating with gas release. However, for the limited range of tests conducted, the parameters selected are adequate for describing the observed gas-release fractions.

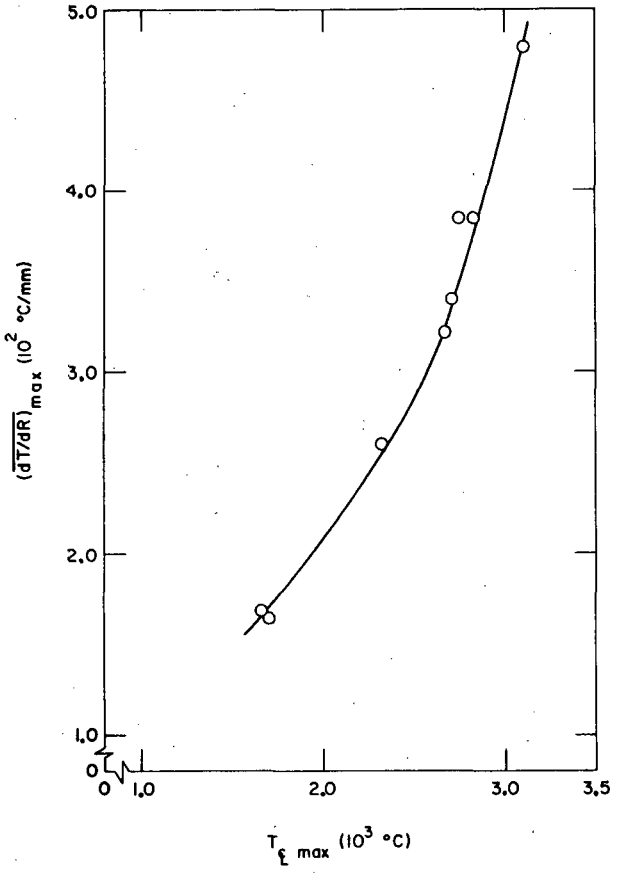

Fig. 8. Relationship between Maximum Centerline Temperature and Maximum Volume-averaged Temperature Gradient for PCM-type Tests. ANL Neg. No. 306-77-316.

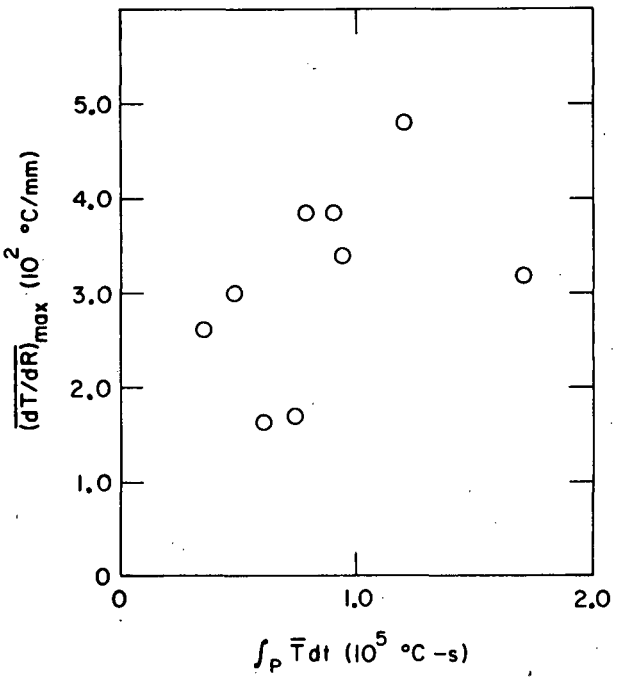

Fig. 9. Maximum Volume-averaged Temperature Gradient as a Function of Time Integral of Volume-averaged Temperature. ANL Neg. No. 306-77-315.

2. Relationships between Gas Release and Temperature-history Parameters

Calculated thermal-history parameters (and the quantitative stereology measurements discussed in Sec. III.B) for nine DEH experiments are tabulated in Table VI. The transient-temperature histories are still being evaluated for the remaining tests. The confidence intervals indicated were determined by assuming that the calculated values of $\bar{T}$ and T_{CL} were in error by ±200°C. The possible sources of error in the temperature calculations are discussed in the appendix.

TABLE VI. Thermal-history Parameters and Quantitative Stereology Results for PCM-type Tests

Test No.	Xenon Release, %	$\int \bar{T}\,dt$, 10^5 °C·s		$\int_p T_{CL}\,dt$, 10^5 °C·s	$\int (\overline{dT/dR})\,dt$, 10^4 °C·s/mm		$\left(\frac{\overline{dT}}{dR}\right)_{max}$, 10^2 °C/mm	$T_{CL_{max}}$, °C	V_v^P	Percent Swelling	$S_v^{\alpha P}$, 10^2 mm^2/mm^3	$\left(S_g^{\alpha P}\right)^{xs}$, 10^4 mm^2/g
		Power on	Total		Power on	Total						
9	12.6											
16	2.3											
18	8.2											
21	44 ± 1								0.224	25.0	4.06	4.12
22	13.1 ± 0.5	0.482	0.697	0.75	0.684	1.012	3.01	2510	0.155	14.8	3.32	2.93
23	1-5	0.354	0.524	0.47	0.464	0.717	2.60	2320				
24	12.0 ± 0.5	0.780	1.121	1.12	1.203	1.787	3.85	2830	0.137	12.4	2.60	2.10
25	42.9 ± 3.9											
26[a]	59 ± 2	1.2	1.4	1.55	1.7	2.2	4.8	3100	0.264	31.8	4.31	4.69
27	33.3 ± 0.7	0.897	1.166	1.07	1.421	1.854	3.85	2740				
28									0.132	11.8	2.36	1.83
29	2.0 ± 0.6	0.613	0.738	0.86	0.869	1.024	1.65	1700	0.030	0	0.69	0
30	0.4 ± 0.1	0.735	0.909	0.92	0.890	1.093	1.69	1660				
31	20.1 ± 1.5											
32	16.1 ± 2.4	0.934	1.150	1.32	1.151	1.538	3.40	2700	0.179	18.1	3.00	2.68
33	42.6 ± 2.2	1.697	2.046	2.09	2.326	2.818	3.22	2660				

[a]Calculated temperature parameters for test 26 are based on estimated surface-temperature histories.

Percentage xenon release is plotted against $\int_p \bar{T}\,dt$ in Fig. 10 and against $(\overline{dT/dR})_{max}$ in Fig. 11. A general trend of higher gas-release fractions at higher values of $\int_p \bar{T}\,dt$ is observed (see Fig. 10), although a large amount of scatter is evident. Gas release correlates more strongly with $(\overline{dT/dR})_{max}$, as shown in Fig. 11. The data suggest that there is a threshold value of temperature gradient, ~3 x 10^2 °C/mm, above which large amounts of gas release are observed. Because there is an empirical correlation between TCL_{max} and $(\overline{dT/dR})_{max}$, a relationship also exists between xenon release and TCL_{max}. This relationship, plotted in Fig. 12, shows a rapid increase in gas release for centerline temperatures above 2500°C.

B. Relationships between Gas Release and Microstructural Change

During DEH testing of the Robinson fuel, a complex sequence or sequences of microstructural changes occurred that resulted in the formation of extensive networks of interconnected, intergranular porosity. The network provided escape paths for much of the fission gas that was able to diffuse to the grain boundaries. Quantitative relationships have been developed that link

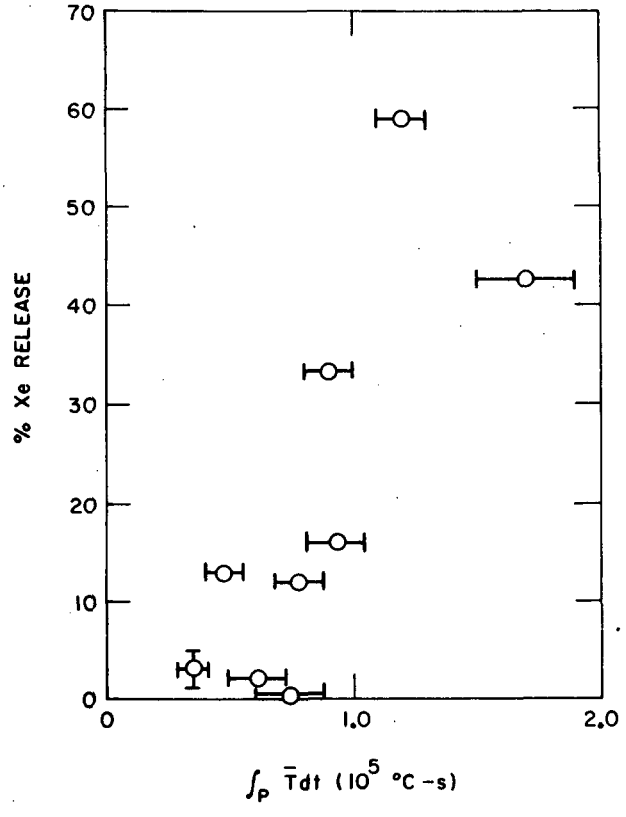

Fig. 10. Percent Xenon Release as a Function of Time Integral of Volume-averaged Temperature. ANL Neg. No. 306-77-318.

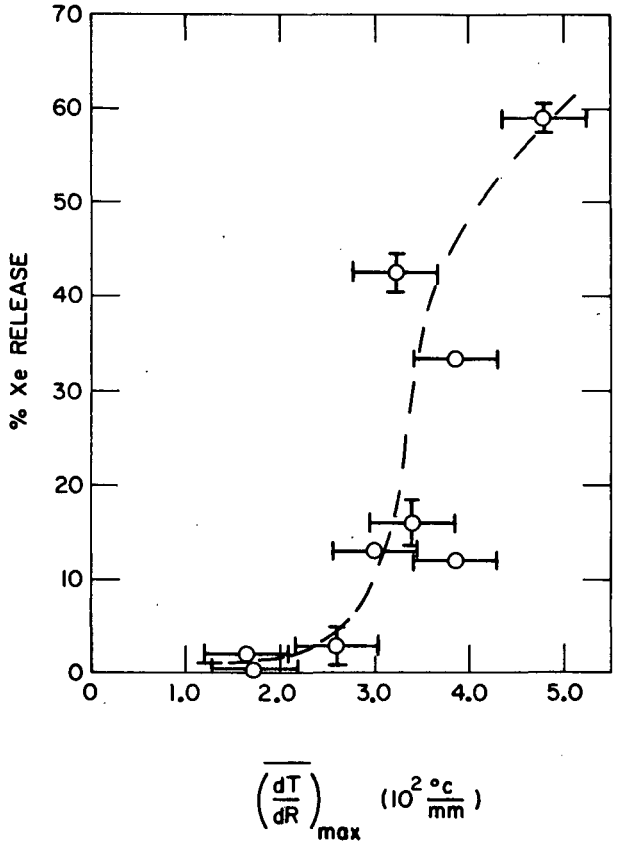

Fig. 11. Percent Xenon Release as a Function of Maximum Volume-averaged Temperature Gradient. ANL Neg. No. 306-77-311.

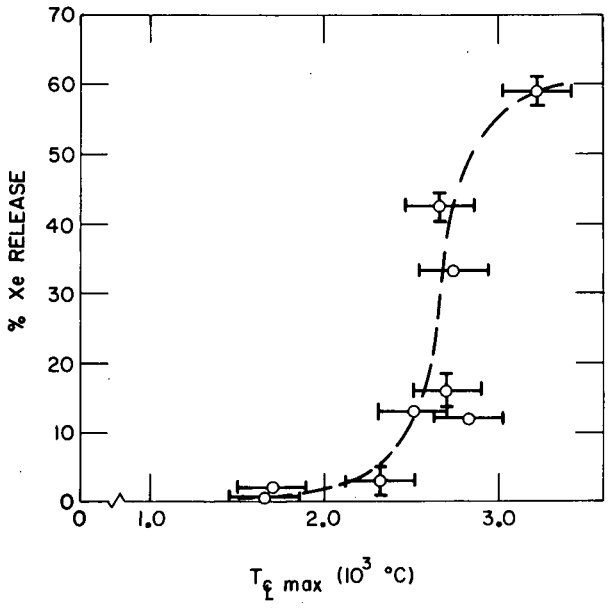

Fig. 12. Percent Xenon Release as a Function of Maximum Centerline Temperature. ANL Neg. No. 306-77-322.

fission-gas release with the transient-induced microstructural changes. Before these relationships are presented, the as-irradiated microstructure and the observed microstructural changes will be described both qualitatively and quantitatively.

1. The As-irradiated Microstructure

During irradiation, the density of the Robinson fuel increased from the as-fabricated value of 92% to a final density of 94% of theoretical. Approximately half the porosity in the irradiated fuel is in the form of large, roughly spherical pores with diameters in the range 0.03-0.25 mm. These pores, formed during fabrication, were apparently not altered during irradiation. Examples of this kind of porosity are visible in the polished plane section through an as-irradiated fuel pellet shown in Fig. 13. Most of the remaining porosity consists of isolated intergranular pores that are too small to be visible at the magnification of Fig. 13. These pores, shown in Fig. 14, range in size from 0.5 to 2.0 μm and have a specific surface area of 69 mm^2/mm^3. The fine-scale pores are remnants of the as-fabricated porosity after in-pile densification.

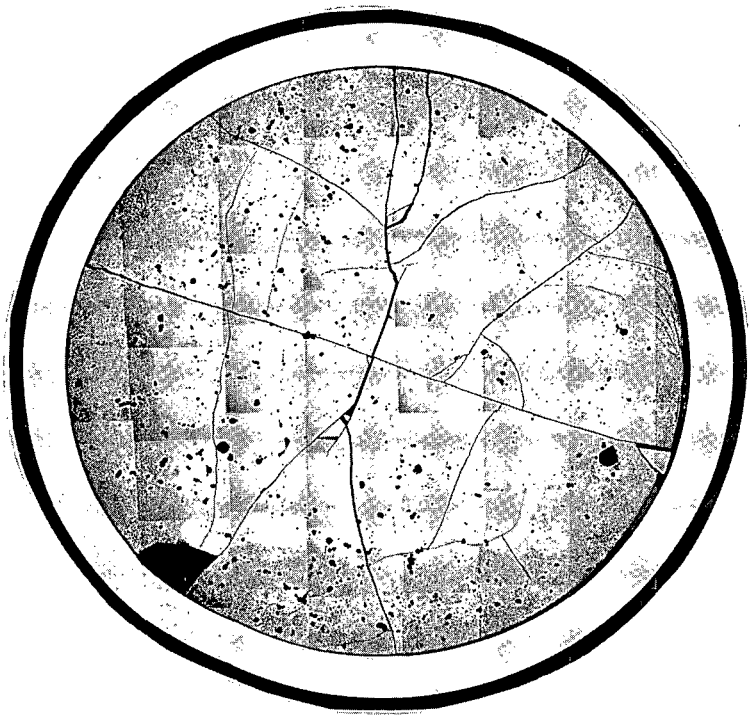

Fig. 13

Transverse Section through an As-irradiated Robinson Pellet. Neg. No. MSD-185339.

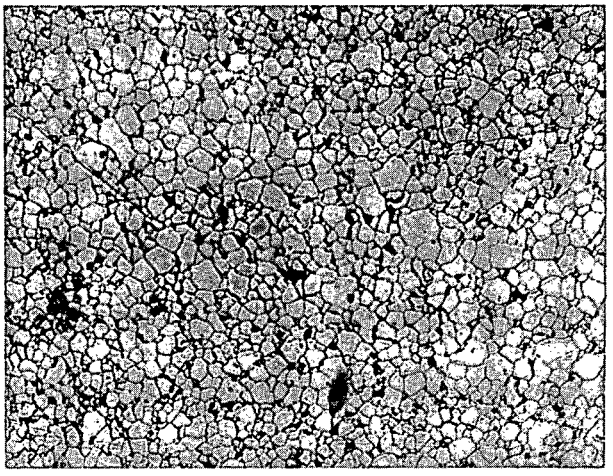

Fig. 14

Grain Structure and Fine-scale Porosity in As-irradiated Robinson Fuel. Neg. No. MSD-190434.

Intra- and intergranular fission-gas bubbles with diameters between 10 and 50 nm were also present in the as-irradiated structure. Rough estimates of the density of fission-gas bubbles from replica fractographs of the type shown in Figs. 15 and 16 gave values of 10^{10} to 10^{11} bubbles/mm^3.

2. Microstructural Changes during DEH Transients

The most striking feature of the post-DEH microstructure is the pattern of intergranular separations that occur in the hotter portions of the fuel. Intergranular separations are present in the unmelted regions of specimens in which central melting occurred and in some of the specimens in which there was no melting.

Examples of the various morphologies identified as directional and nondirectional intergranular separations are shown in Fig. 17. The initial stages in the formation of directional and nondirectional patterns of intergranular separations are shown in Figs. 17A and 17B, respectively. These separations are cracklike in appearance. The patterns of intergranular separation are nearly fully developed in Figs. 17C and 17D. Note that, for both the directional and nondirectional patterns, almost every grain is adjacent to a separation, and the separations are interlinked over long distances through the structure. Examples of varying degrees of development of both classes of intergranular separation are present in a single test specimen.

In some cases, as shown in Fig. 17E, wide variations in the amount of directionality occurred over distances of ~100 μm. For individual test specimens, an appreciable degree of directionality was present in 40% of the area that showed intergranular separations. Directional separations tended to be oriented perpendicular to the pellet radius. However, the local orientation direction was influenced by the presence of stress concentrators, such as large pores and cracks, and near contact points between pellet fragments. The density of intergranular separations also increased in the vicinity of sources of stress concentration.

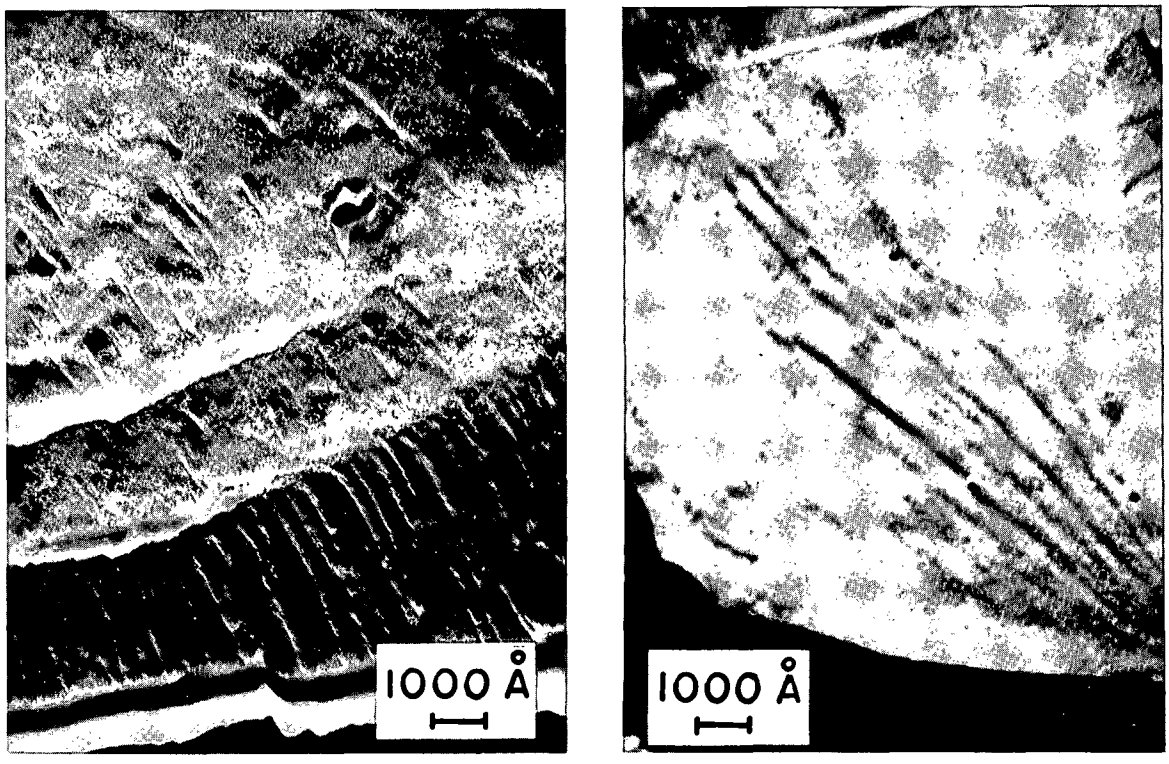

Fig. 15. Intragranular Fission-gas Bubbles in As-received Robinson Fuel. Neg. No. MSD-185902.

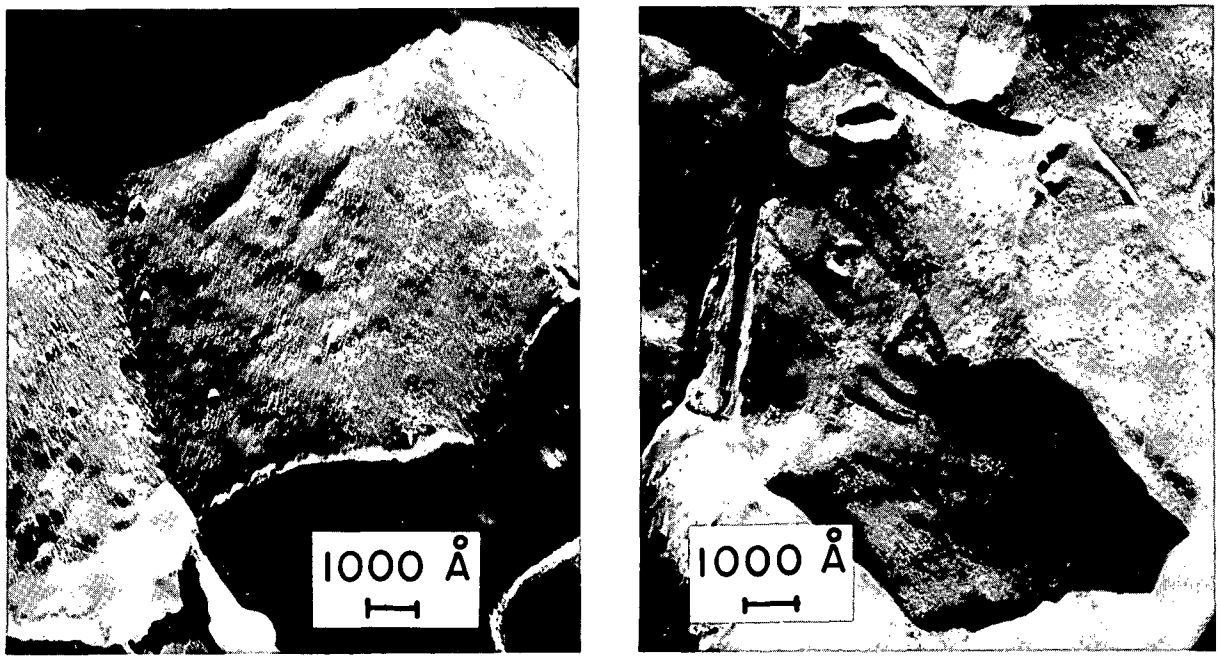

Fig. 16. Intergranular Fission-gas Bubbles in As-received Robinson Fuel. Neg. No. MSD-185901.

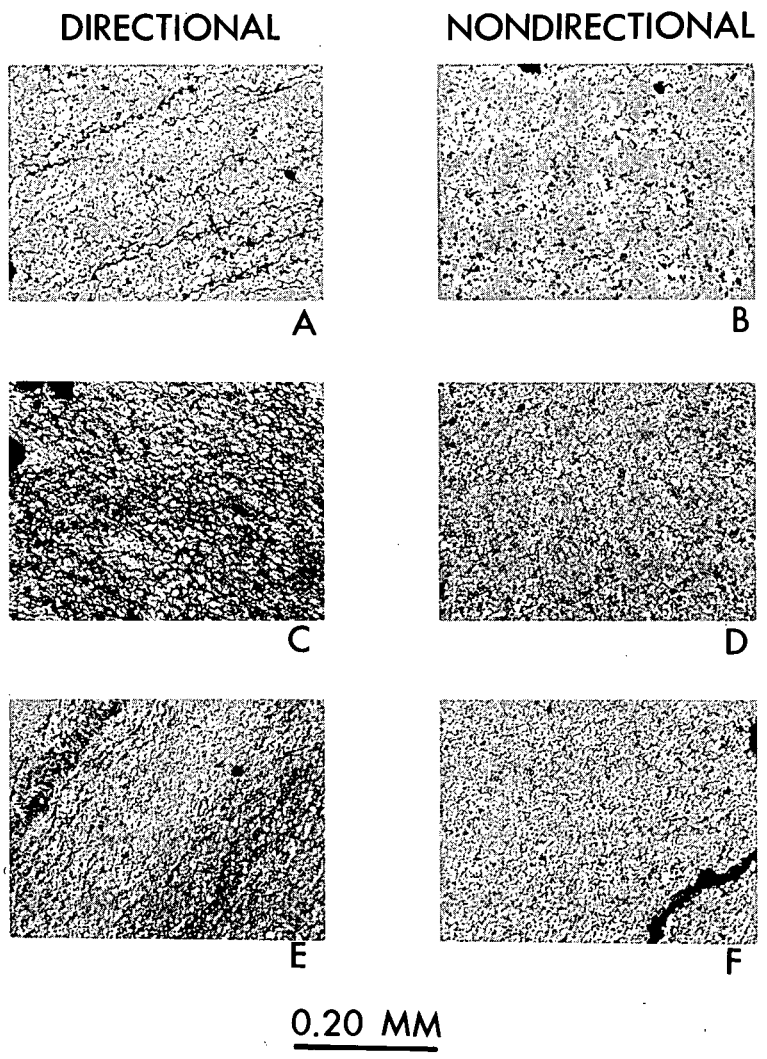

Fig. 17. Optical Micrographs of Intergranular Separations in DEH-tested Fuel. Neg. No. MSD-190928.

Varying amounts of plastic deformation of the grains are associated with the separations, especially in the hotter portions of the fuel. Examples of grains in which plastic flow has occurred are shown in Fig. 17E. The characteristics exhibited in Figs. 17A-17E indicate that mechanical stresses are at least partly responsible for the formation of the intergranular separations.

A final example of a form of intergranular separation, shown in Fig. 17F, was present in fuel that was heated to temperatures close to the melting point. These separations occupy grain boundaries of all orientations with equal frequency. The rounded outline of these features contrasts with the sharper edges and cracklike appearance of the separations shown in Figs. 17A-17E. The structure shown in Fig. 17F is characteristic of high-temperature grain-boundary swelling.

Evidence that fission-gas effects were in part responsible for the formation of the separations was obtained by examining the posttest microstructure in the scanning electron microscope (SEM). Specimens were prepared by fracturing DEH-tested specimens at room temperature. Figure 18 shows a series of micrographs along a radial traverse of the specimen from test 24. Radial temperature profiles at various times during this test are shown in Fig. 6. At the outermost radial positions (see Figs. 18A and 18B), intergranular fracture predominated. The grain surfaces are covered with fission-gas bubbles that range in size from the limit of resolution (~30 nm) to ~50 nm. Where transgranular fracture occurred, no bubbles are visible. A marked increase in bubble size and density (values of $\sim 10^{13}$ bubbles/mm^3 were determined for the area in Fig. 18A) has occurred over the as-irradiated microstructures shown in Figs. 15 and 16. Average bubble size increases toward the center of the pellet, i.e., where transient temperatures were higher, as shown in Figs. 18C and 18D. When the bubbles reach 0.2 μm in diameter, continued bubble coalescence results in the formation of sinuous grain-surface channels, as may be seen in Figs. 18C-18E.

Grain-boundary-channel formation and bubble growth appear to proceed at different rates on individual grain faces, even for faces on the same grain. The arrow in Fig. 18F indicates a grain face on which the channels have coalesced to form a nearly complete separation between two adjacent grains. More extensive grain-boundary separation has occurred at the location shown in Fig. 18G. At this position, the predominant fracture mode has changed to transgranular. Note that, in addition to the intergranular separations, intragranular bubbles with diameters of 0.1-0.3 μm are present. This sequence of micrographs shows how intergranular separations may be formed by a mechanism involving growth and coalescence of fission-gas bubbles.

The term "intergranular porosity," as used in the rest of this report, collectively signifies the intergranular bubbles, channels on grain faces and edges, and planar separations observed in the posttest examinations.

The extent of the intergranular separations can be quantitatively characterized by measuring the pore volume fraction, V_v^P, and pore-solid surface area, $S_v^{\alpha P}$, as a function of radial position. Quantitative stereology techniques were used for the characterization. The measurements were performed on optical micrographs and include features greater than 0.5 μm in size. If pretest values of V_v^P and $S_v^{\alpha P}$ are also known, the volume increase (i.e., swelling) and the new pore-solid surface area produced during the transient can be calculated.

Radial profiles of swelling and new surface area per gram of fuel, $(S_g^{\alpha P})^{xs}$, are plotted in Fig. 19. These graphs show that the radial gradients are quite large and that, for some tests, the maximum surface-area increase may occur at an intermediate radial position. A cross-plot of $(S_g^{\alpha P})^{xs}$ against percent swelling (see Fig. 20) shows that a single relationship describes the data for several radial positions in each of seven DEH tests.

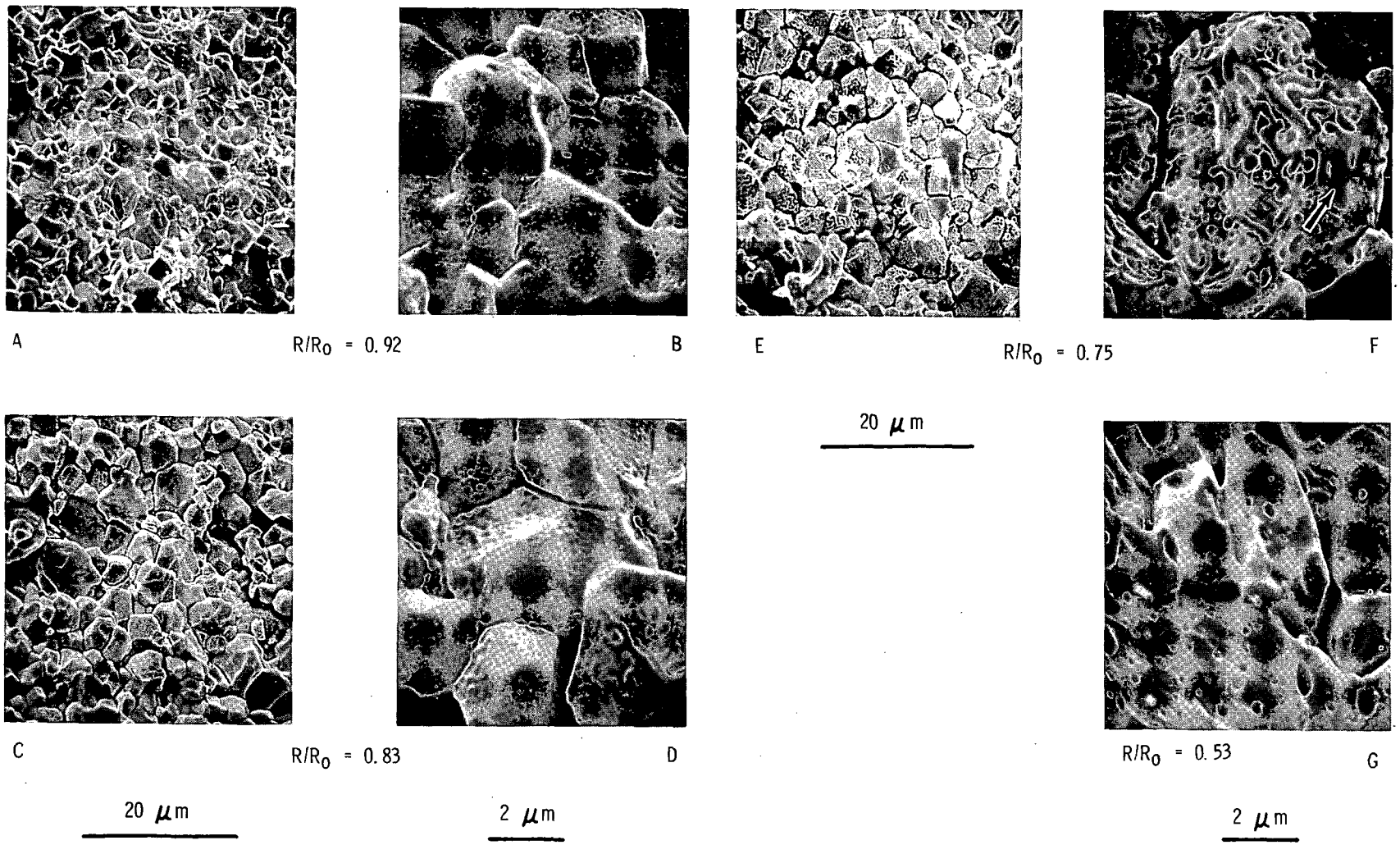

Fig. 18. Scanning Electron Fractographs at Four Radial Positions in a Robinson Fuel Pellet after DEH Test 24. Neg. No. MSD-190926.

Fig. 18 (Contd.). Neg. No. MSD-190925.

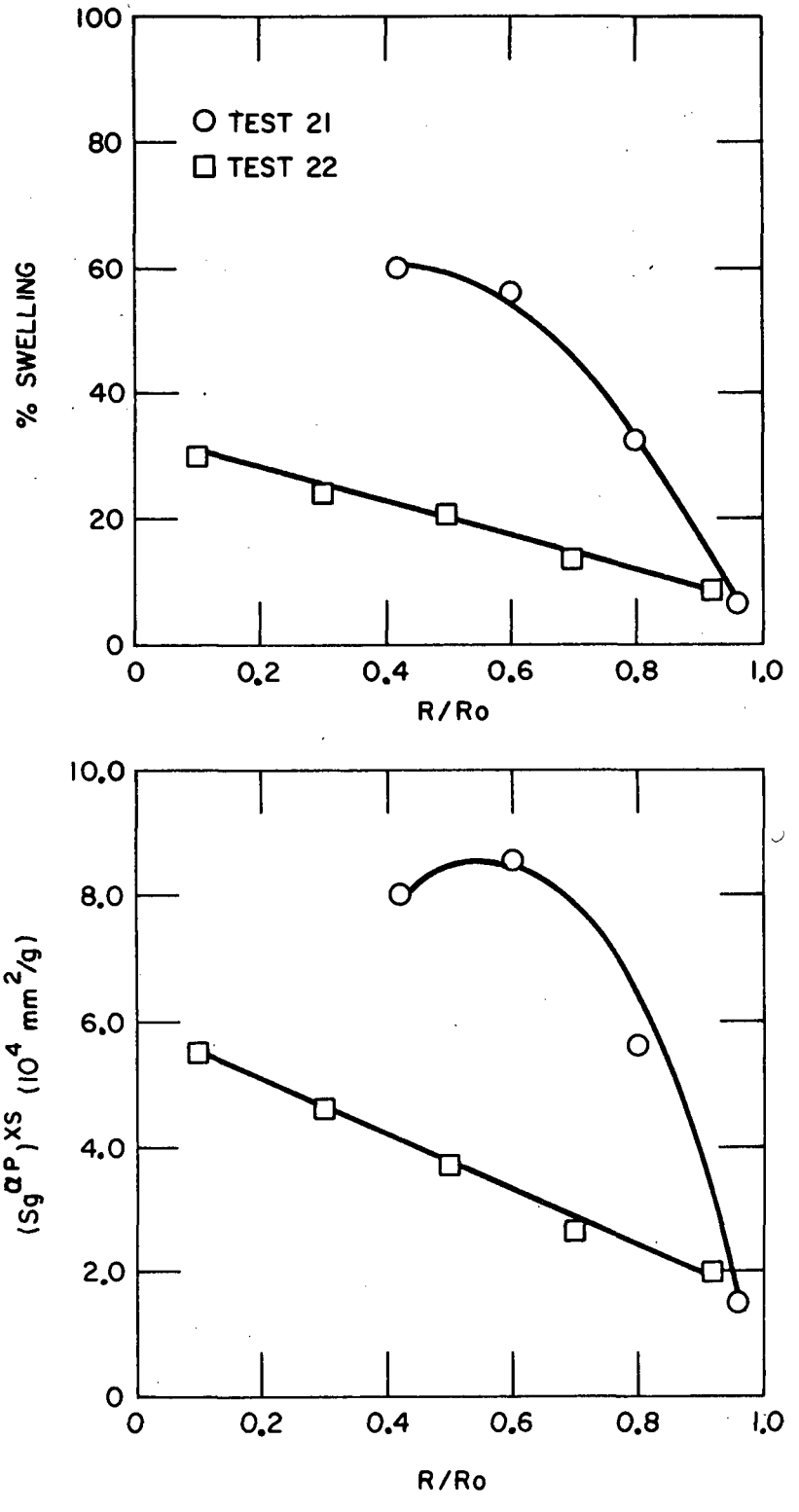

Fig. 19. Radial Profiles of Swelling and Pore-solid Surface Area Produced by DEH. ANL Neg. No. 306-77-317.

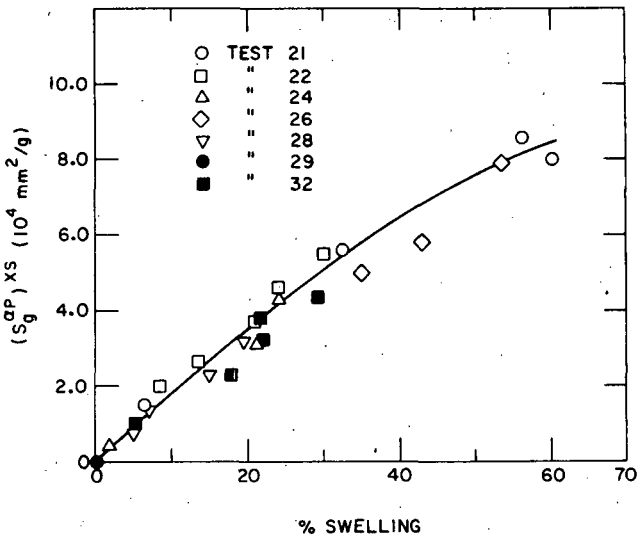

Fig. 20. New Pore-solid Surface Area vs Percent Swelling for Several Radial Positions in Seven DEH-tested Pellets. ANL Neg. No. 306-77-319.

Volume-averaging of the radial profiles of swelling and $(S_g^{\alpha P})^{xs}$ was used to calculate the quantitative stereology parameters listed in Table VI for seven DEH tests. The volume-averaged parameters were also used for the quantitative relationships between gas release and microstructural change developed in Sec. III.B.3.

3. Relationships between Gas Release and Microstructural Change

Since there is a direct and nearly linear relationship between $(S_g^{\alpha P})^{xs}$ and the amount of swelling, as shown in Fig. 20, a relationship between gas release and swelling will have nearly the same form as a relationship between gas release and surface area. Therefore, to avoid repetition, we will discuss only the relationship between gas release and swelling. Plots of xenon release against both V_v^P and swelling are presented in Figs. 21 and 22. The significance of the similarity of the two plots arises from the fact that the initial and final microstructural conditions must be known to calculate swelling,

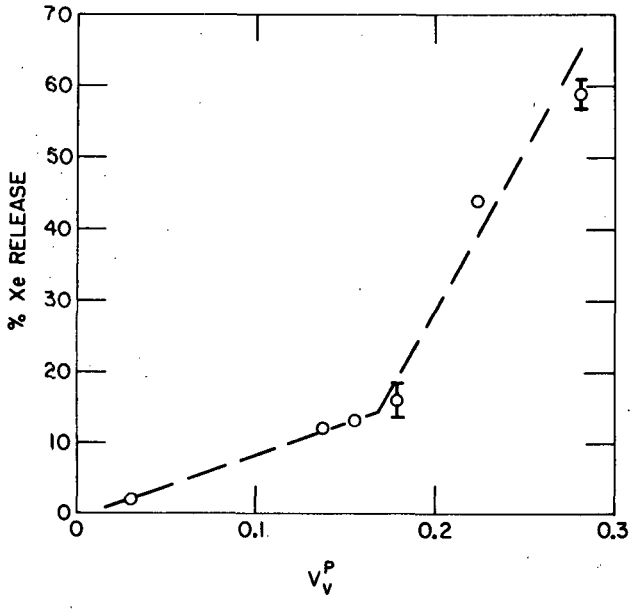

Fig. 21. Percent Xenon Release as a Function of Post-DEH Volume-averaged Pore Volume Fraction. ANL Neg. No. 306-77-313.

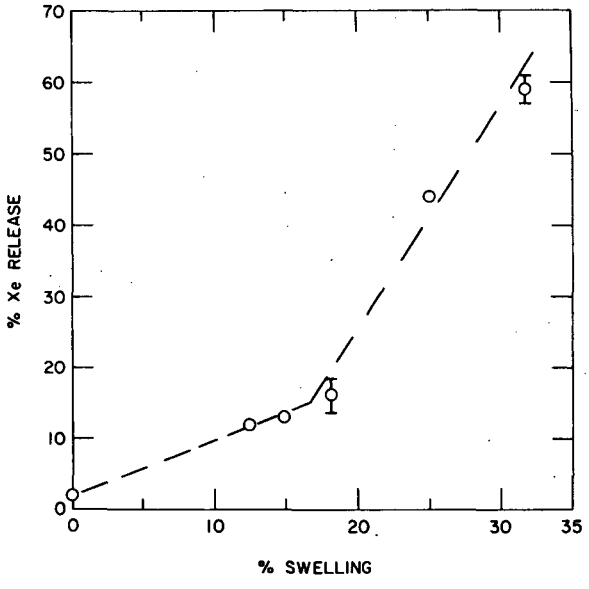

Fig. 22. Percent Xenon Release as a Function of Volume-averaged Swelling. ANL Neg. No. 306-77-310.

while V_v^P is a measure of the final microstructural state only. Comparison of Figs. 21 and 22 indicates that no information is lost by plotting xenon release against a parameter that measures only the final microstructural state. Figure 22 shows that ~2% gas release was obtained without any microstructural change.

For tests in which swelling was less than 17-19%, an approximately linear increase in gas release with swelling was observed. For larger swelling values, the percentage gas release increased more rapidly with increasing swelling. The slope change in the curve for percent Xe release versus percent swelling is believed to be the result of the rapid interlinkage of the intergranular porosity when the pore volume fraction reaches a critical value. The interlinked porosity allows fission gas on grain edges and boundaries to escape. For swelling below the critical value, gas release is believed to occur mainly by diffusional mechanisms.

This explanation is consistent with studies of percolation probabilities, in which extensive long-range interconnection of a second phase in a matrix is predicted if the volume fraction of the second phase exceeds a critical value.[10-12] Interconnection of the second-phase particles is negligible for volume fractions less than the critical value. Critical volume fractions of 0.17, 0.20, and 0.36 have been reported in Refs. 10-12, respectively. In these studies, the critical volume fractions were observed to be a function of the size distribution and shape of the second-phase particles. Figure 21 suggests that the critical volume fraction for the interconnection of the intergranular porosity is 0.17-0.19, which is within the range of reported values.

IV. DISCUSSION OF RESULTS

A. Gas-release Mechanisms

Empirical correlations were developed between gas release and transient-temperature history and between gas release and microstructural change for the initial series of PCM-type tests that suggest some preliminary conclusions about the mechanisms of gas release.

The relationships between gas release and maximum temperature parameters contrast with the weaker dependence of gas release on the integral parameters (see Fig. 10). Appreciable scatter was observed for the PCM-type tests for which the test conditions were similar. For tests that cover a wider range of initial conditions and heating rates, an even larger amount of scatter would be expected. Since the integral or time-at-temperature parameters determine the extent to which diffusional processes occur, the weak relationships between gas release and the integral parameters suggest that diffusional processes are not the only mechanisms that affect gas release. This conclusion is supported by GRASS-SST calculations,[13] which underpredict the measured gas releases when only diffusional processes are considered.

The results of the present study indicate that the mechanisms responsible for the formation of interlinked grain-surface and edge channels (see Fig. 18) and interlinked planar separations (see Fig. 17) can operate in series with intragranular bubble diffusion to transport fission gases from the grain interiors to the pellet surface. A preliminary indication of the nature of these mechanisms can be obtained from an interpretation of the transient-induced microstructural changes.

The series of micrographs in Fig. 18 indicates that intergranular separations can form by the diffusion-controlled processes of growth and coalescence of fission-gas bubbles. However, optical micrographs of areas in the same specimen (Fig. 23) show that extensive cracklike intergranular separations are present at radial positions where the predominant features on the intergranular fracture surfaces are isolated fission-gas bubbles. That is, the gradual processes of bubble growth and coalescence to form channels and of channel coalescence to form separations can be interrupted by the more rapid process of crack propagation. The stresses responsible for cracking are the result of the applied axial load, differential thermal expansion, and the pressurization of intergranular fission-gas bubbles.

The intergranular propagation of the cracks is, in part, due to the reduction in grain-grain contact area by the intergranular fission-gas bubbles. Crack propagation is accompanied by varying amounts of plastic flow in the adjacent grains, depending on the local temperature. For temperatures close to the melting point, stresses are relieved by plastic flow without cracking,

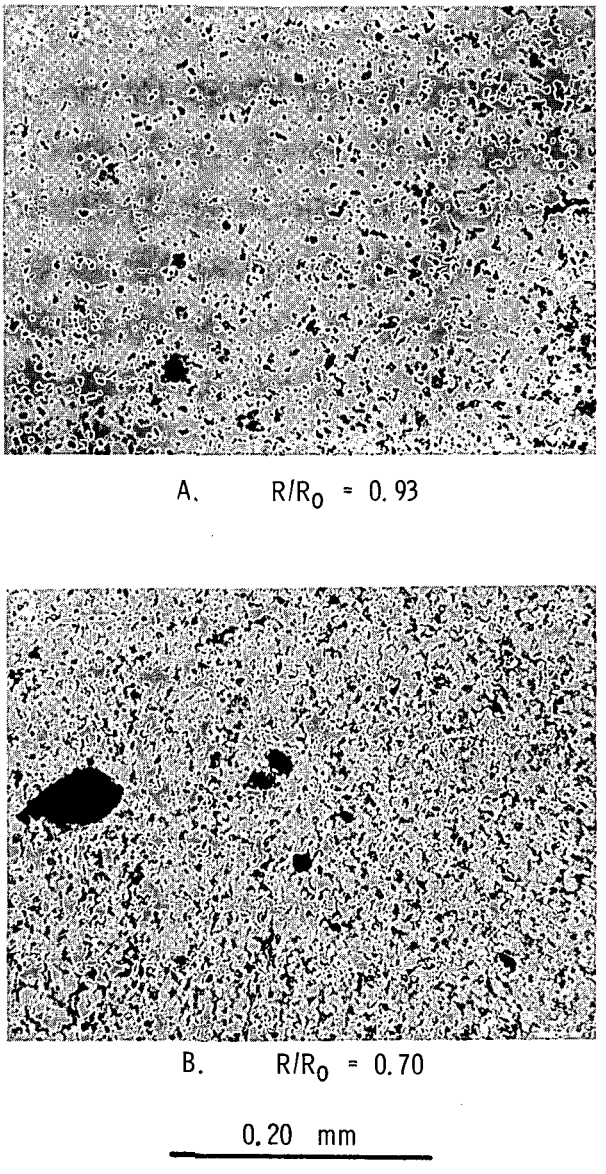

Fig. 23. Optical Micrographs of a Polished Section at Selected Radial Positions in a Robinson-fuel Pellet after DEH Test 24. Compare with the scanning electron fractographs in Fig. 18. Neg. No. MSD-190927.

and the bubble- and channel-coalescence processes are largely responsible for intergranular separation. Therefore, the formation of the network of intergranular porosity responsible for transient fission-gas release is apparently a result of both diffusion-controlled (bubble growth and coalescence) and mechanical (cracking) mechanisms.

The importance of the intergranular porosity indicates that its formation and interlinkage should be considered in the computer modeling of transient fission-gas release. However, a complete, physically realistic treatment of the planar intergranular separations would require a detailed mechanical model for crack formation and propagation. The GRASS-SST code does not contain such a model. However, the formation of the grain-face and -edge channels, shown in Figs. 18C-18F, and the venting of the channels to the fuel exterior are modeled in GRASS-SST. At present, these models do not account for rapid, long-range interlinkage of the channels after a critical value of swelling has been reached. The measured and GRASS-predicted gas-release fractions can be compared if the calculated grain-boundary and -edge gas burdens are assumed to be released by the interlinkage of the intergranular porosity. As shown in Fig. 24, the GRASS-SST calculations performed under this assumption are in good agreement with the measured gas-release fractions. The straight line in Fig. 24 represents perfect correspondence between the predicted and measured values.

As a further check on the validity of the assumption of complete release of the grain-edge gas, the calculated posttest gas distributions were compared with the observed radial profiles of volume swelling. This comparison is based on Fig. 22, which indicates that interlinkage of the intergranular porosity occurs if the volume-averaged swelling exceeds ~18%. It is reasonable to apply

the same critical swelling value to the question of determining the radial limit of interlinkage within a single pellet. That is, for a plot of volume swelling versus radius (e.g., Fig. 19), interlinkage is assumed only for radial positions smaller than the radius at which the volume swelling equals 18%. Since interlinkage is thought to be negligible at larger radii, gas on the grain boundaries and edges in these regions is trapped, not released. The assumption used for the GRASS-SST calculations, i.e., total release of the grain-boundary and -edge gas, can be tested by evaluating the amount of gas on boundaries and edges in the regions for which negligible interlinkage occurred.

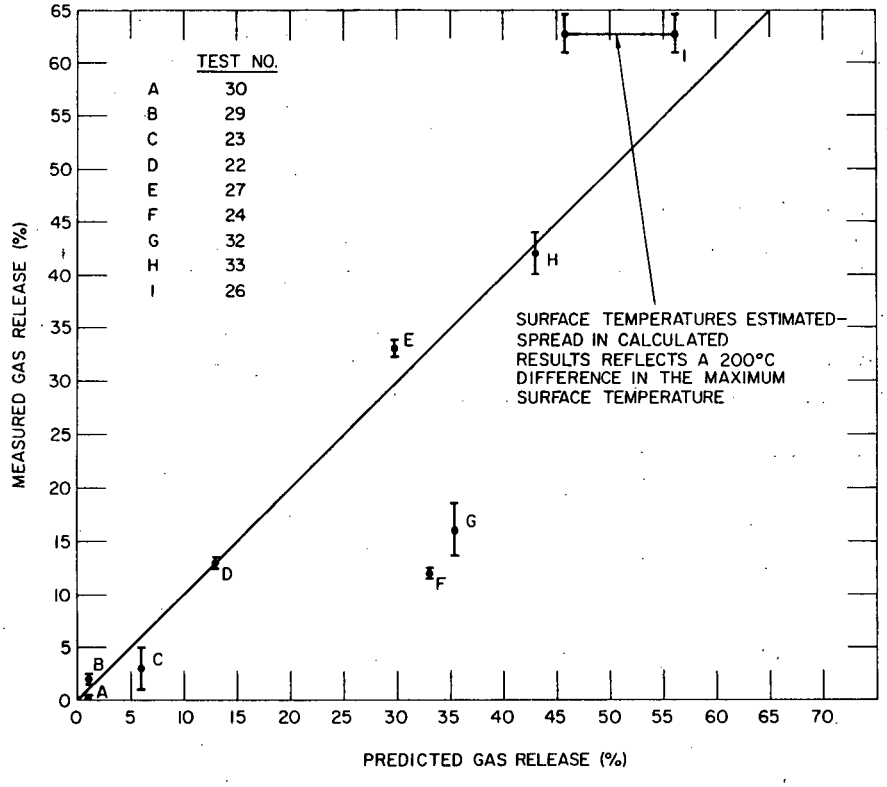

Fig. 24. Experimentally Measured vs GRASS-predicted Gas Releases, Assuming That All Grain-edge Gas Is Vented. ANL Neg. No. 306-77-320.

As shown in Table VII, the boundary and edge gas in the noninterlinked regions is, in all cases, a small percentage of the GRASS-SST-calculated gas

TABLE VII. Comparison of GRASS-calculated Boundary and Edge Gas with a Simple Interlinkage Criterion

Test	Radial Limit of Interlinkage (fractional radius)	Boundary and Edge Gas Outside of Interlinked Region (% of total calculated release)
22	0.58	1.1
24	0.68	0.76
26	0.91	0.16
32	0.80	0.47

release. Therefore, the assumption of total release of the boundary and edge gas yields a good approximation to the release expected on the basis of a simple interlinkage model. No simple explanation exists for the discrepancies between the predicted and measured gas releases for tests 24 and 32. However, GRASS-SST analyses indicate that improvements in the bubble movement models may be required to give better prediction of the gas releases for these tests.

The overall agreement of the predicted with measured gas-release values shown in Fig. 24, coupled with the relatively poor correlation obtained when only diffusional mechanisms are considered,[13] provides additional evidence that the interlinkage of intergranular porosity is an important gas-release mechanism.

B. Relation to Nuclear-heated Transient Tests

Intergranular separations similar to those described for the DEH-tested Robinson fuel are present in the irradiated PWR fuel tested in the film-boiling region of rod 007 from the PBF IE-1 test. Figure 25 shows the appearance of the separations on polished plane sections through DEH- and PBF-tested fuel. The extent of directional separation formation is less in the PBF-tested fuel, but the separations were otherwise similar. Scanning electron fractographs

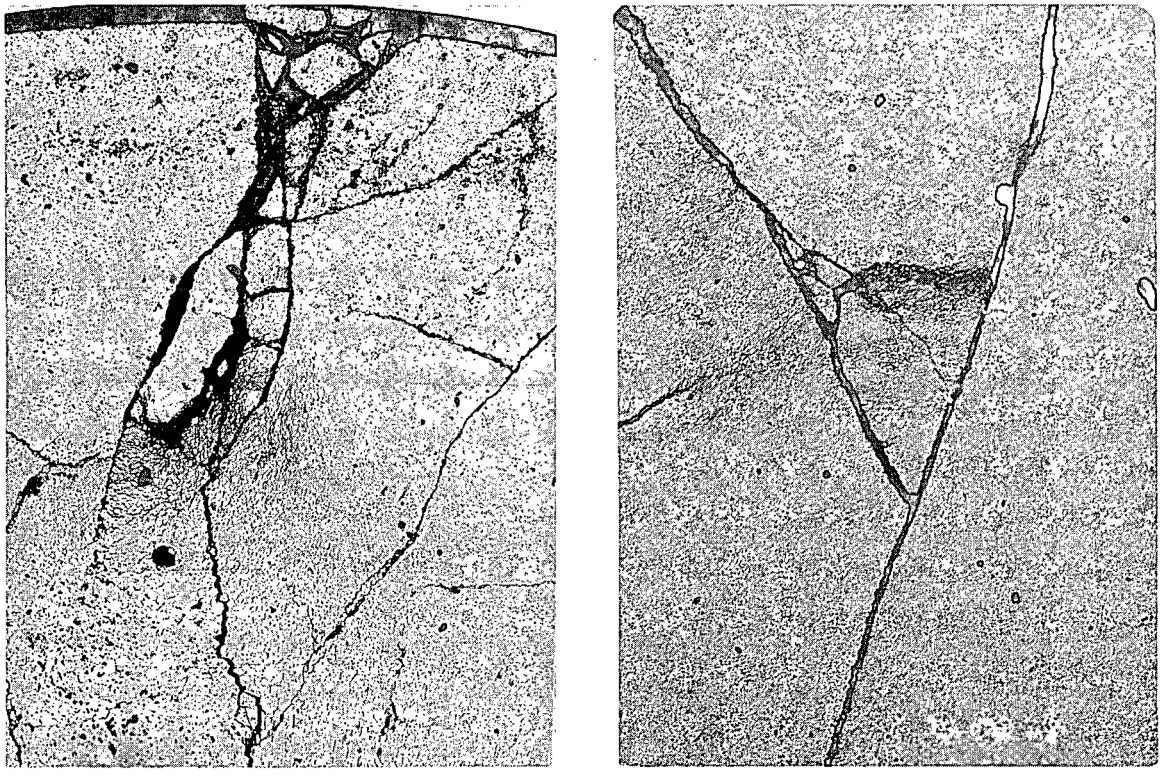

a. PBF–tested b. DEH–tested

0.2 mm

Fig. 25. Intergranular Separations in PBF– and DEH–tested Fuel. ANL Neg. No. 306–77–162.

of Saxton fuel from the film boiling region of rod 007 of the PBF IE-1 test (Figs. 26A-26C) show features that are nearly identical to those observed for DEH tests of Robinson fuel and presented in Fig. 18. The intergranular fractures in Fig. 26D exposed grains that have almost completely separated from their neighbors. An isolated contact area is visible only in the center of this region. This nearly complete separation explains a grain-pullout problem experienced in the metallographic preparation of specimens from rod 007.[14]

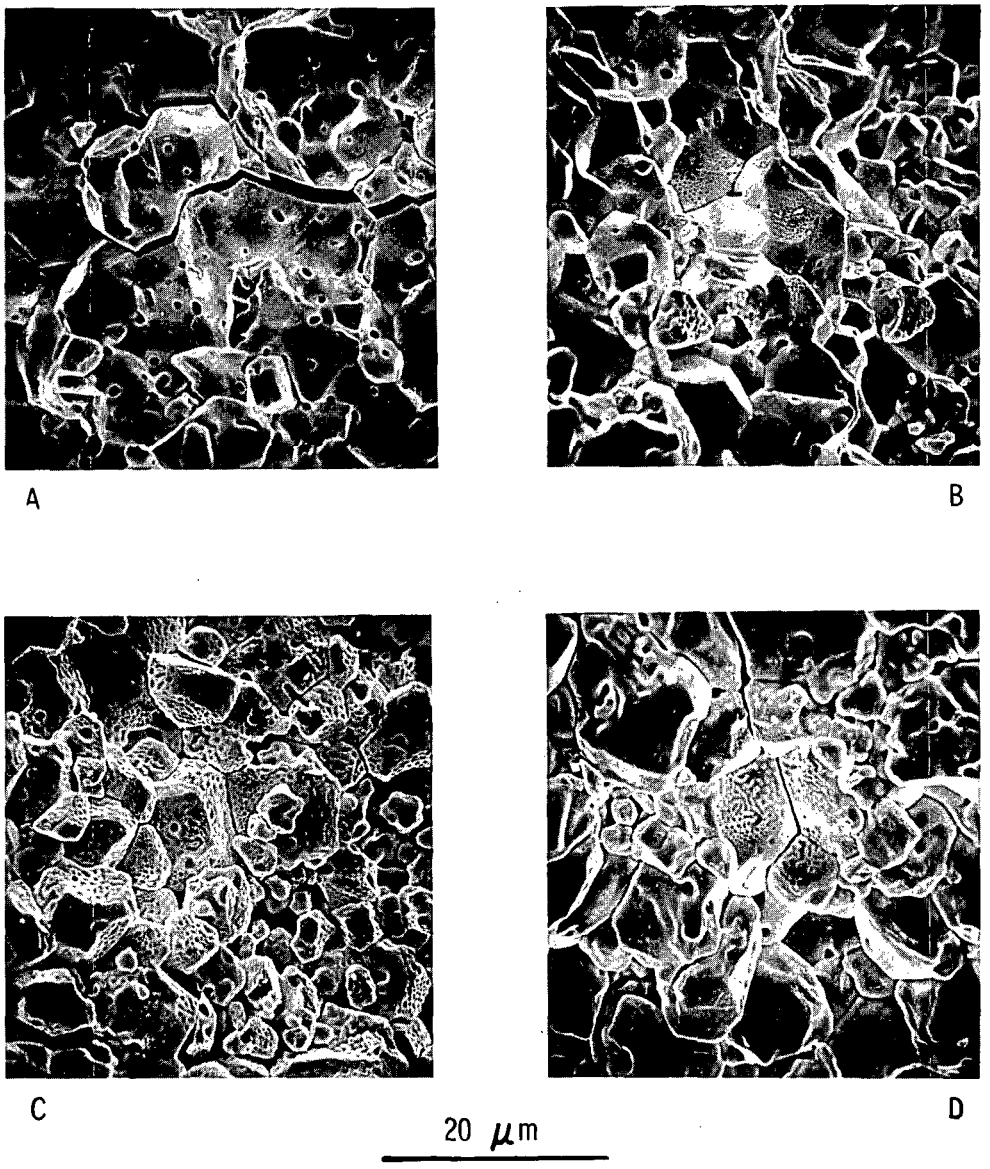

Fig. 26. Scanning Electron Fractographs of Fuel from Film-boiling Region of Rod 007 from PBF IE-1 Test. Compare with Fig. 18. Neg. No. MSD-190924.

The series of photos in Fig. 26 shows that the intergranular separations in the PBF IE-1 test were formed by the growth and coalescence of fission-gas bubbles to form grain-boundary channels and the coalescence of channels to

completely separate the faces of adjacent grains, the same sequence of events observed for the DEH-tested Robinson fuel. Rapid, discontinuous formation of intergranular separations by crack propagation also occurred during the PBF test, as evidenced by the cracklike directional separations in the PBF-tested fuel. However, since the density of directional separations was lower for the PBF-tested fuel, intergranular separation by crack propagation was probably not as prevalent as in the DEH-tested material.

The similarity of the intergranular separations obtained under electrical and nuclear heating conditions demonstrates that the DEH technique can simulate many of the effects of in-reactor transient heating. Since gas release during DEH transients is related to the formation of intergranular porosity a similar correlation probably exists for nuclear heating.

The radial constraint supplied by the Zircaloy cladding during most in-reactor transients was absent during the present series of DEH tests. The resulting differences in stress state probably account for the higher incidence of directional intergranular separations in the DEH-tested material. The question of the effect of stress state on transient gas release has not yet been resolved. However, this problem can be studied by DEH tests in which the fuel is radially constrained with a close-fitting, electrically insulating sleeve. The results in this report may be applicable to accident scenarios in which the cladding is not in contact with the fuel, e.g., if the cladding has ballooned.

APPENDIX

Calculation of Transient Radial Temperature Profiles

Transient-temperature histories for DEH tests are calculated by solving the time-dependent heat-transfer equation with the DEHTTD code. The code contains expressions taken from the literature for the temperature dependence of thermal and electrical conductivity of UO_2, and requires as input the time histories of pellet voltage, current, power, and surface temperature. The radial temperature profile at the start of the transient is obtained by solving the steady-state heat-transfer equation for the input values at time zero. Note that, because voltage, current, and power are input to the code and electrical conductivity is known, the problem is overdetermined. The code uses the extra information to adjust the electrical-conductivity expression until a convergence criterion is met in a solution of the steady-state problem. The electrical conductivity is altered by incrementing a variable called STOICH, which affects the electrical conductivity in the same way as fuel stoichiometry in the conductivity expressions of Aronson et al.[15] Note that the variable STOICH is not the same as stoichiometry. STOICH accounts for effects such as fuel chemistry and microstructure in addition to stoichiometry. The value of STOICH obtained for the steady-state solution is carried over for the use in the transient solutions of the heat-transfer equation.

The available literature expressions for thermal and electrical conductivity, i.e., the expressions used in the code, are appropriate for high-density, high-purity UO_2. There are no comparable data for high-burnup fuel. In addition, the microstructure is continually changing during the DEH test as intergranular separations are formed. As a result, attempts at calculating temperature profiles of Robinson-fuel specimens using the literature data gave centerline temperatures that were in error by as much as 600°C. A comprehensive solution to this problem, e.g., by detailed physical-property measurements on high-burnup fuel, was beyond the scope of the program. At the same time, some corrective measures were necessary. The problem was addressed by identifying two factors considered most likely to cause the observed errors.

The first factor was the discrepancy between the literature values of electrical conductivity and the measured values for the Robinson fuel. The resistance of pellet stacks is routinely monitored during the initial preheat period before DEH testing. Therefore, the effective electrical conductivity of the stacks, which consist of a high-burnup fuel pellet sandwiched between two depleted-UO_2 pellets, is easily determined. The measured conductivity values were fitted to an equation of the form

$$\sigma = \frac{A}{T} \exp\left(-\frac{B}{T}\right),$$

where σ is electrical conductivity, T is absolute temperature, and A and B are constants. At 300°C, the measured conductivities were approximately two orders of magnitude greater than the literature value used in the code. At 1000°C, the difference was approximately a factor of 3. The empirically determined electrical conductivities were incorporated into the DEHTTD code by adding a term to the existing expression. Because the empirical term was significant only at low temperatures, and because the STOICH term already in the code gave a partial correction for the difference in electrical conductivity, the effect on calculations of radial temperature profiles was negligible.

The second factor thought likely to affect the accuracy of the heat-transfer calculation was the change in thermal conductivity during the transient caused by the formation of intergranular separations. Preliminary studies indicated that the calculated temperature profiles were sensitive to small changes in thermal conductivity and relatively insensitive to changes in electrical conductivity. Furthermore, the preliminary studies indicated that it was necessary to account for the decrease in thermal conductivity caused by the formation of intergranular separations during the transients.

The effect of intergranular separations was modeled by introducing a cracking factor into the thermal-conductivity equation to give an expression of the form

$$T_k' = (1 - F)T_k,$$

where F is the cracking factor, T_k is the literature value of thermal conductivity, and T_k' is the modified value used for temperature-profile calculation. The cracking factor is time-dependent, has a value of zero at the start of transient heating, and increases linearly with time to a maximum value at the time of maximum power input.

The maximum value of the cracking factor is an adjustable parameter. For a physically realistic treatment, the maximum cracking factor would be a function of the extent of intergranular separation that occurs during each transient. For the calculations presented in this report, the maximum cracking factor for all tests was assumed to be 0.5. This value was determined by a trial-and-error matching of the calculated centerline temperature for test 24 to the melting temperature of UO_2 (2850°C). This value was chosen because the posttest examination of the microstructure of test 24 revealed that the center of the fuel pellet had been heated to incipient melting. With a cracking factor of 0.5, the maximum centerline temperature calculated for test 24 was 2824°C, which closely matched the microstructural result. In addition, using a maximum cracking factor of 0.5, the code accurately predicted the melt radius obtained in test 26.

These correlations indicate that the use of the cracking factor allows accurate calculations of the transient radial temperature profiles. However, because the maximum cracking factor was held constant for all tests, the calculated temperatures may be in error for the tests in which small amounts of intergranular separation occurred. To account for possible errors arising from this source, the temperature-history parameters in Table VI have confidence intervals that assume potential errors in T_{CL} and $\bar{T}$ calculations of as much as 200°C. The resulting uncertainty in $(\overline{dT/dR})_{max}$ values range from 9 to 25%. Sensitivity studies indicate that the probable errors are in the range 50-150°C. Continued refinement of the calculated temperatures can be obtained by developing a relationship between the maximum cracking factor and a measure of intergranular separation, such as swelling or surface area.

Finally, the uncertainty in the temperature profiles calculated by the DEHTTD code compares favorably with the uncertainties in standard temperature calculations performed for in-reactor fuel rods.

REFERENCES

1. *The Role of Fission Gas Release in Reactor Licensing*, NUREG-75/077, Core Performance Branch, U. S. Nuclear Regulatory Commission (Nov 1975).
2. C. E. Beyer and C. R. Hann, *Prediction of Fission Gas Release from UO_2 Fuel*, BNWL-1875 (Nov 1974).
3. D. Freund and W. Schikarski, *Der Direkt Elektrish Geheizte UO_2 Brennstab*, KFK-1031, EURFNR-773 (1970).
4. J. Rest, M. G. Seitz, S. M. Gehl, and L. R. Kelman, "Development and Experimental Verification of SST-GRASS: A Steady-state and Transient Fuel Response and Fission-product Release Code," *Proc. CSNI Specialists Meeting on Behavior of Water Reactor Fuel Elements under Accident Conditions*, Spätind, Norway (Sept 13-16, 1976).
5. Personal communication, P. E. MacDonald, ANC, to L. R. Kelman, ANL (Sept 11, 1975).
6. R. A. Lorenz, J. L. Collins, and S. R. Manning, *Quarterly Progress Report on Fission Product Release from LWR Fuel for the Period Oct.-Dec. 1975*, ORNL/TM-5290 (Mar 1976).
7. B. J. Wrona and E. W. Johanson, *Development of Direct Electrical Heating Apparatus to Study the Response of Nuclear Fuel to Applied Transients*, Nucl. Technol. *29*, 433 (1976).
8. J. T. Dusek, ANL, private communication (1975).
9. J. C. Vogelwede, ANL, private communication (1976).
10. F. Forscher, *Analysis of Continuity of One Phase in a Powder Mixture of Two Phases*, J. Franklin Inst. *259*, 107-14 (1955).
11. T. H. Blakely and A. E. S. White, in *Plansee Proc. 2nd Seminar, Routte/Tyrol.*, ed. by F. Benesousky, pp. 335-45, Pergamon Press, London (1956).
12. J. Gurland, *An Estimate of Contact and Continuity of Dispersions in Opaque Samples*, Trans. Met. Soc. AIME *236*, 642-46 (1966).
13. J. Rest, M. G. Seitz, and S. M. Gehl, *Release of Fission Gas from High-burnup Fuel During Transient Heating*, Trans. Am. Nucl. Soc. *26*, 320-24 (1977).
14. Personal communication, S. M. Gehl, ANL, to J. G. Crocker, EG&G (Apr 12, 1977).
15. S. Aronson, J. E. Rulli, and B. E. Schaner, *Electrical Properties of Non-stoichiometric Uranium Dioxide*, J. Chem. Phys. *35*, 1382-88 (1961).